Applied Surface Science 684 (2025) 161884

Contents lists available at ScienceDirect

Applied Surface Science

journal homepage: www.elsevier.com/locate/apsusc

Full Length Article

Novel thermally conductive coating for cotton fabrics based on reduced graphene oxide decorated with *in situ* synthesized silver nanoparticles

Giacomo Mandriota [a,1], Adriana Grandolfo [a,b,c,1], Raffaella Striani [d], Annamaria Panniello [a], Giuseppe V. Bianco [e], Antonella Milella [b], Claudio Mele [d], Roberto Comparelli [a], Antonio Greco [d], Marinella Striccoli [a], Elisabetta Fanizza [a,b], Gianpiero Colangelo [d], M. Lucia Curri [a,b,*], Chiara Ingrosso [a,*], Carola Esposito Corcione [d,*]

[a] CNR-IPCF c/o Department of Chemistry University of Bari Aldo Moro, Via Orabona, 4, Bari 70125, Italy
[b] Department of Chemistry, University of Bari Aldo Moro, Via Orabona, 4, Bari 70125, Italy
[c] Department of Electrical and Information Engineering, Polytechnic of Bari, Via Amendola 126/b, Bari 70126, Italy
[d] Department of Engineering for Innovation, University of Salento, Via per Monteroni, Lecce 73100, Italy
[e] CNR-NANOTEC, c/o University of Bari Aldo Moro, Via Orabona 4, Bari I-70126, Italy

ARTICLE INFO

Keywords:
Cotton fabrics
Reduced graphene oxide
Ag nanoparticles
Histidine linker
Hybrid nanocomposite coating
Thermal conductivity

ABSTRACT

The application of thermally conductive materials as coating on fiber surfaces represents an innovative technology solution for conveying heat dissipation capability to IR-opaque textiles. In this work, a sustainable and scalable approach to manufacture a hybrid nanocomposite coating for cotton, formed by Reduced Graphene Oxide (RGO) sheets functionalized by histidine (His) and decorated by Ag nanoparticles (NPs), is reported for increasing thermal conductivity of cotton fabrics. Tens nm in size Ag NPs were synthesized, *in situ,* at the coordinating sites of the His-RGO modified cotton impregnated by H_2O/CH_3OH solutions of the $AgNO_3$ precursor, under UV-light exposure, without using chemical reductants. The physical chemical properties of the nanocomposite modified fabrics were comprehensively investigated, integrating chemical, structural and morphological analysis, with characterizations of their thermal, electrical, oxygen permeability, surface wettability and mechanical properties. Thermal conductivity of cotton was measured by Differential Scanning calorimetry (DSC) technique, which was here validated by Transient Plane Source (TPS) method, assessing the effectiveness of DSC in measuring thermal conductivity of textiles. The resulting coating exhibits a thermal conductivity, which was twice as high as untreated cotton, maintaining its breathability, increasing its flexibility, while simultaneously reducing its wettability. This notable enhancement can be attributed to the synergistic effect of the conductive Ag nanostructures formed among the His-RGO sheets within the nanocomposite, and it matches the thermal conductivity achieved by current state-of-the-art methods, while offering additional advantages of being more eco-friendly, scalable, and sustainable. The reported characterization of the structural properties of the achieved coating opens the venue to interesting perspectives towards its application in passive conducting cooling textiles for personal thermal comfort management.

1. Introduction

Recently, increasing attention has been devoted to innovative strategies aiming to engineer textiles to fulfill technological demands to overcome lack of functionalities of traditional ones and conveying additional properties, like hydrophobicity, flame retardancy, self-cleaning, antimicrobial, electric and thermal conductivity, anti-wrinkle, antistatic and UV radiation shielding [1–4]. Nanostructured materials and nanocomposites, showing high surface to volume ratio, along with original chemical and physical properties depending on

* Corresponding authors at: Department of Chemistry University of Bari Aldo Moro, via Orabona 4, Bari 70125, Italy (M.L. Curri). CNR-IPCF c/o Department of Chemistry University of Bari Aldo Moro, via Orabona 4, Bari 70125, Italy (C. Ingrosso). Department of Engineering for Innovation, University of Salento, Via per Monteroni, Lecce 73100, Italy (C.E. Corcione).
E-mail addresses: marialucia.curri@uniba.it (M.L. Curri), c.ingrosso@ba.ipcf.cnr.it (C. Ingrosso), carola.corcione@unisalento.it (C.E. Corcione).
[1] These authors contributed equally to this work.

https://doi.org/10.1016/j.apsusc.2024.161884
Received 6 August 2024; Received in revised form 14 November 2024; Accepted 20 November 2024
Available online 23 November 2024
0169-4332/Published by Elsevier B.V. This is an open access article under the CC BY-NC-ND license (http://creativecommons.org/licenses/by-nc-nd/4.0/).

morphology and chemical composition [5,6], are optimal candidates for effectively conveying to fabrics novel functionalities, without detrimentally affecting their breathability or texture.

In this frame, textiles featuring advanced thermoregulatory characteristics have been regarded as original solutions for accomplishing human thermal comfort, addressing the need of high-performance textiles in industries such as sports, medical, and aerospace, where thermal management is crucial [7,8]. Among these, passive cooling textiles, which are designed to enhance human body heat dissipation through the fabrics without consuming extra energy [9], manage personal thermal comfort by regulating heat exchange between skin and surrounding environment, by enhancing transmission of mid infrared radiation, decreasing near infrared radiation absorption, and increasing human body heat loss by thermal conduction [10].

To the best of our knowledge, few studies have focused on engineering textiles and patches for fulling such a challenge, and each one offers an innovative solution, exhibiting concomitantly, however, limitations as well. Among these, some approaches report on the fabrication of textiles with high thermal conductivity, where heat conduction inside an IR-opaque textile is the primary heat dissipation pathway; some routes consist of coating, by impregnation, natural textiles as cotton, which is favored for its softness, wear comfort and breathability, with high thermally conductive nanofillers or their formulations with polymers. As for example, cotton has been modified by impregnation with carbon nanotubes [11], with polymer formulations based on epicholorohydrin based resin modified by thermally conductive nanostructures like carbon nanotubes, boron nitride nanosheets (BNNSs), and graphene derivatives [12–14], and formulations formed of graphene nanoplatelets and BNNSs embedded in polyurethane (PU) [15–17]. Although these routes are the simplest and the most scalable ones, accomplishing a significant improvement in thermal conductivity, their scaling up is challenged, because of the unsafe use of hazardous precursors in the PU synthesis and toxic byproducts from epichlorohydrin-based resins [18]. As an alternative to these issues, few approaches have used formulations of biocompatible polymers heavily loaded with high thermally conductive nanofillers, but are however limited to the fabrication of patches and use of fossil-fuel based polymers, and, in some cases, also toxic organic solvents. As an example, polymer nanocomposites based on BNNSs embedded into polyvinylalcohol (PVA)/dimethyl sulfoxide formulations have been fabricated into fibers through a hot-drawn 3D printing process, and the resulting patches have a thermal conductivity increased up to 0.078 $Wm^{-1}{\cdot}K^{-1}$, which is 2.2 times higher than cotton and 1.6 times higher than neat PVA fabrics [19]. As an alternative, few other works have focused on fabricating patches formed of biodegradable polymers heavily loaded with high thermally conductive nanostructures. In this regard, patches of cellulose/alkaline/urea solutions modified with 60 wt% edge-selective hydroxylated BNNSs, achieved through wet-spinning and weaving, have reached a thermal conductivity increase from 0.86 $Wm^{-1}\ K^{-1}$ up to 2.914 $Wm^{-1}\ K^{-1}$ [20]. Also, silk fibroin patches, loaded with 50 wt% exfoliated BNNSs reached 1.77 $Wm^{-1}\ K^{-1}$ using vacuum filtration, have been developed [21]. Despite being eco-friendly, these last methods necessitate costly fabrication technologies and a high concentration of nanofillers, which exhibit chemical inertness and strong interlayer interactions, limiting sustainability and scalability of the approach.

From this picture it therefore emerges that the development of passive cooling textiles by ecofriendly and sustainable approaches is still an unsolved challenge. In this work, a thermally conductive coating based on modified cotton was prepared by impregnation with a nanocomposite formed of histidine functionalized Reduced Graphene Oxide (His-RGO) *in situ* decorated with Ag nanoparticles (NPs). RGO possesses the thermal conductivity closest to that of monolayer graphene, which ranges from $370 - 600\ W\ m^{-1}K^{-1}$ when supported onto a substrate [22], and compared to BNNSs, it has a higher chemical reactivity affording superior exfoliation and chemical modification capability, opening the venue to technologies that do not solely encompass a good conductivity, but exploit also the functionalities of molecular species anchored onto its basal plane.

His was selected as a biocompatible exfoliating agent of RGO, enabling its dispersion in water [23,24]. His binds RGO by aromatic π-π stacking interactions, without introducing additional structural defects, detrimental for its thermal and electrical conductivity [25], and grafts RGO with $–COO^-$ and imidazole nitrogen functionalities, effective in coordinating nanostructures [26].

RGO sheets were decorated with NPs of Ag, which is characterized by high thermal conductivity ($429\ W\ m^{-1}K^{-1}$) [27], as able in principle to improve interlayer heat diffusion, bridging adjacent RGO sheets [28]. These coatings were achieved through *in situ* photoreduction via UV-light irradiation of His-RGO coated fabrics soaked in $AgNO_3$ aqueous methanol solutions [29,30], a method proven successful in decorating cotton with Ag NPs for commercial antimicrobial textiles [29,30], demonstrating viability in terms of scalability and sustainability. This approach circumvents the requirement of using strong and hazardous reductants (e.g., $NaBH_4$) or even milder alternatives (e.g., citrate, ascorbic acid), which all necessitate time-consuming washing steps to optimize thermal conduction.

The thermal conductivity of the cotton fabrics was measured by Differential Scanning Colorimetry (DSC). Such a method, that, to the best of our knowledge, has been applied for measuring the thermal conductivity of insulating materials such as polymers, glasses and ceramics [31,32], and has never been reported so far for textiles, was applied here to cotton fabrics, with the validation of the Transient Plane Source approach (TPS).

2. Materials and methods

2.1. Chemicals and materials

Reduced Graphene Oxide (RGO) was purchased from Graphene Supermarket (1.6 μm thick flakes), histidine (His) from Alpha Aesar, methanol ($CH_3OH \geq 99.9$ %), acetone (99.9 %) and silver nitrate ($AgNO_3$, > 99 %) from Sigma Aldrich. All these chemicals were used as received without further purification. Aqueous solutions were prepared by using Milli-Q water (18.2 MΩ·cm, organic carbon content $\geq 4\ \mu g\ L^{-1}$) achieved by a Milli-Q gradient A-10 system.

2.2. Exfoliation and functionalization of RGO by His

100 mg of RGO powder were stirred in 100 mL of His aqueous solutions (1.6 mg mL^{-1}), at room temperature, for allowing its intercalation among and functionalization of the sheets [23,24]. Then, the His-RGO dispersion was purified from the excess of His by four cycles of ultracentrifugation (45000 rpm for 30 min), sonicated in water at pH 11 in an ice cooled US bath for 5 h, and then purified by two and four cycles of ultracentrifugation (45000 rpm for 30 min). Finally, the isolated His-RGO powder was dispersed in water at neutral pH, at a concentration of 4 mg ml^{-1} and sonicated for 6 h.

2.3. Pre-treatment of cotton (Cot)

Cot fabrics were washed to remove contaminants from the fibers by stirring in acetone for 8 h, followed by three cycles of washing in water at 40 °C, alternating each one by a drying step onto a hotplate at 50 °C [33].

2.4. Modification of Cot fabrics with His-RGO (Cot/His-RGO)

Cot fabrics were impregnated with 4 mg ml^{-1} His-RGO aqueous dispersions at neutral pH, by two dipping steps of 3 h, followed by overnight dipping, and finally, by others two dipping steps of 3 h. Each dipping step was followed by drying at 50 °C onto a hotplate. These samples are called Cot/His-RGO (Table 1).

Table 1
Samples investigated in the work.

Sample	UV-light exposure	$AgNO_3$ (g mL^{-1})	H_2O (mL)	CH_3OH (mL)
Cot/His-RGO	No	––	––	––
Cot/His-RGO$_{1:1,UV}$	Yes	––	5	5
Cot/His-RGO/Ag$_{1:1}$	No	0.1	5	5
Cot/His-RGO/Ag$_{1:1,UV}$	Yes	0.1	5	5
Cot/His-RGO$_{9:1,UV}$	Yes	––	9	1
Cot/His-RGO/Ag$_{9:1,UV}$	Yes	0.1	9	1

2.5. Preparation of the Ag NPs coated Cot/His-RGO fabrics (Cot/His-RGO/Ag)

The *in situ* synthesis of the Ag NPs onto the Cot/His-RGO fabrics was performed soaking overnight the fabrics in 0.1 g mL^{-1} $AgNO_3$ water/methanol mixed solutions, at two different water/methanol volume ratio, namely 9:1 v/v and 1:1 v/v, and then, the Ag^+ ions were allowed to reduce onto the wet Cot/His-RGO fabrics in air and under UV-light irradiation [29,30] ($\lambda = 254$ nm, 0.2 mW cm^{-2}) for 30 min. The samples were placed 10 cm orthogonally from the UV-light lamp source. These samples were named Cot/His-RGO/Ag$_{9:1,UV}$ and Cot/His-RGO/Ag$_{1:1,UV}$, respectively (Table 1). As a purpose of comparison, Cot/His-RGO samples, wet in 9:1 v/v and 1:1 v/v water/methanol mixtures and exposed to UV-light irradiation, as well as Cot/His-RGO samples impregnated by 0.1 g mL^{-1} $AgNO_3$ 1:1 v/v water/methanol mixed solutions, dried in dark conditions at ambient atmosphere, were investigated. These samples are named Cot/His-RGO$_{9:1,UV}$, Cot/His-RGO$_{1:1,UV}$ and Cot/His-RGO/Ag$_{1:1}$, respectively (Table 1).

2.6. Characterization techniques

UV–Vis absorption spectra in reflectance mode were collected at room temperature by means of a Cary 5000 (Varian) UV/Vis/NIR spectrophotometer equipped with an integration sphere to measure the Diffuse Reflectance. Raman spectra were recorded by using a LabRAM HR Horiba-Jobin Yvon spectrometer with an excitation wavelength of 532 nm. Measurements were carried out under ambient conditions at low laser power (1 mW) to avoid laser-induced damage of the sample. The Raman signal from the silicon wafer at 520 cm^{-1} was used to calibrate the spectrometer and accuracy of the spectral measurement was 1 cm^{-1}. X-Rays Photoelectron Spectroscopy (XPS) analyses were carried out with a Scanning XPS Microprobe (PHI 5000 Versa Probe II, Physical Electronics) equipped with a monochromatic Al Kα X-ray source (1486.6 eV), operating at 15 kV and 24.8 W, with a spot size of 100 μm. Survey (0–1200 eV) and high-resolution spectra (C1s, O1s, N1s and Ag3d) were recorded in FAT (Fixed Analyser Transmission) mode at a pass energy of 117.40 eV and 29.35 eV, respectively. All spectra were collected at an angle of 45° with respect to the sample surface. Charging was compensated using a dual beam charge neutralization system with a flux of low energy electrons (~1 eV) combined with very low energy positive Ar^+ ions (10 eV). The hydrocarbon component of C1s spectrum was used as internal standard for charging correction and it was fixed at 285.0 eV. Best-fitting of the high-resolution spectra was carried out with MultiPak data processing software (Physical Electronics). Attenuated Total Reflection Fourier Transform Infrared (ATR-FTIR) spectroscopy was carried out by a 670 FTIR spectrometer (Varian, Palo Alto, CA, USA) equipped with a diamond ATR accessory of 2 mm and a deuterated tryglicine sulfate (DTGS) detector. Samples were drop-cast on the internal reflection element and solvent was allowed to evaporate. Spectra were recorded in the range of 4000–400 cm^{-1}, acquiring 16 scans with a nominal resolution of 1 cm^{-1}. Transmission Electron Microscopy (TEM) analyses were performed by a Jeol Jem-1011 microscope operating at 100 kV, equipped by a high-contrast objective lens and a W filament as electron source, with an ultimate point resolution of 0.34 nm. Images were acquired by a Quemesa Olympus CCD 11 Mp Camera. Samples were prepared dipping a 300 mesh amorphous carbon-coated Cu grid in aqueous dispersions of His-RGO, then leaving the solvent to evaporate at room temperature. Field Emission Scanning Electron Microscopy (FE-SEM) measurements were performed by a Zeiss Sigma microscope (Carl Zeiss Co., Oberkochen, Germany) operating in the range of 0.5–20 KV and equipped with an in-lens secondary electron detector and an INCA Energy Dispersive Spectroscopy (EDS) detector. Samples were mounted onto stainless-steel sample holders by a double-sided conductive carbon tape and grounded by silver paste. Size statistical analysis of the Ag nanostructures average size was performed by the ImageJ analysis software.

2.7. Thermal conductivity measurements

Thermal conductivity (TC) was estimated by Differential Scanning Calorimetry (Mettler Toledo TGA/DSC1 Stare System). A sensor material, i.e. Indium (Tm = 156.6 °C) was placed onto the fabrics and heated from 20 °C to 200 °C at 10 °C min^{-1} in nitrogen atmosphere (N_2 flow: 60 ml min^{-1}). Averaged values were obtained by at least three measurements for each sample. For calculating TC, the Flynn and Levin's method [34] was employed and the thermal resistance of the fabric sample (Rs) was defined according to Eq. (1):

$$R_s = R' - R \tag{1}$$

where R′ and R are the thermal resistances determined by the slope of the Indium melting peak with and without the fabric sample, respectively.

TC was estimated according to Eq. (2):

$$TC = \frac{L}{A(R' - R)} = \frac{L}{AR_s} \tag{2}$$

where L is the sample thickness and A is the contact area between the sample and Indium sensor.

The thermal conductivity was also assessed by using a Hot Disk Thermal Constants Analyzer (Hot Disk-TPS 2500S). This equipment measures thermal conductivity within the range 0.005–1800 $Wm^{-1}K^{-1}$, with accuracy better than 5 % and reproducibility better than 1 % by means of Transient Plane Source method (TPS).

The TPS method is based on the heating of a 2-D electrically conducting sensor, that is made in a shape of a spiral, etched out of a thin Nickel foil. This spiral pattern is included in between two thin sheets of Kapton (an insulating material). To make the measurement, the 2-D sensor is fitted between two samples of the same material to be investigated and then an electrical current (with an adjustable intensity) is used to increase the temperature of the sensor, and at the same time recording the electric resistance (that depends on the temperature) increasing as a function of time. In this technique the sensor is used both as the heat source and as a dynamic temperature sensor. The working parameters used for the Hot Disk-TPS 2500S were: temperature 21.0 °C, output power 8 mW, measuring time 4 s, Disk Type Kapton 7577, radius 2.001 mm, TCR 0.004693 K^{-1} and Rs 6.879133 Ω.

2.8. Tensile tests

Mechanical properties of the untreated and treated cotton samples were characterized by a dynamometer (Lloyd LR5K) equipped with a load cell of 100 N, displacement speed of 10 mm min^{-1} and jaw length 40 mm. The fabrics were cut along the texture with size of 120 x 13 x 0.2 mm. Five replicates were performed for each sample. The achieved mean values of tensile strength (σ), strain at break (ε) and tensile modulus (E) were measured.

2.9. Static water contact angle analysis

Static water contact angle (WCA) measurements of untreated and treated cotton fabrics were performed using bi-distilled water (surface tension $\gamma = 72.1$ mN m^{-1}). The analyses were performed at room temperature by means of the sessile drop technique according to NORMAL Protocol 33/89 [35]. Five measurements of each specimen were performed to achieve average values and standard deviation.

2.10. Surface resistivity measurements

Surface Resistivity of cotton fabric was measured according to the American Association of Textile Chemists and Colorists (AATCC) Test Method n. 76–2005 [36]. A parallel plate electrodes configuration was used. The fabric was placed in contact with the electrodes and covered with a corning glass onto which a weight was positioned to apply a constant pressure between the fabric and the electrodes. Resistance between electrodes was measured in both length and width directions of the fabric sample. Surface resistance (Rs) was estimated as:

$$R_s = \frac{R \times W}{D} \quad (3)$$

where R is the measured resistance, W is the width of the fabric and D is the distance between the electrodes.

2.11. Washing durability

Durability of the Cot/His-RGO/Ag$_{1:1,UV}$ samples was assessed by measuring the TC and the static WCA mean values upon 5, 10 and 20 washing cycles of the fabrics with tap water, which were performed by using a centrifuge at the speed of 2000 rpm for 15 min and drying the samples at 60 °C for 3 h.

2.12. Air permeability tests

Oxygen permeability of the neat Cot and of the Cot/His-RGO/Ag$_{1:1,UV}$ samples were measured by means of the Multiperm ExtraSolution instrument (PermTech Srl). The tests were carried out on samples with a 2 cm^2 surface area at 23°C and RH 0 %.

2.13. Atomic force Microscopy (AFM) analyses

The surface topography and roughness of the specimens were examined using a Bruker Multimode 8 atomic force microscope (AFM) in tapping mode under ambient conditions. The images were obtained with scan sizes of 5 × 5 μm^2, and a scan rate of 0.5 Hz. The cantilever employed was a scanasyst-air with a resonance frequency of 70 kHz and a spring constant of 0.4 N m^{-1}. Nanoscope Analysis software version 1.5 was utilized for data processing.

3. Results and discussion

3.1. His-RGO functionalization of cotton fabrics

Commercial Reduced Graphene Oxide (RGO) was exfoliated and functionalized with histidine (His) in water at pH 11 under sonication (Fig. 1a). A purification procedure of the His-RGO dispersion was further performed by ultracentrifugation cycles to remove His in excess (see Materials and methods) [23,24]. The absorption spectra of the supernatants collected after each ultracentrifuge step of the His-RGO dispersion show that the intensity of the absorption shoulder at 275 nm, which is ascribed to the n-π* transition of the His imidazole ring [37] (Fig. S1 of Supplementary material), becomes almost negligible after the third ultracentrifugation cycle, assessing the nearly complete removal of the free His from the His-RGO dispersion.

His is expected to intercalate between the RGO multilayers [26,38] and binds its basal plane via aromatic π–π stacking interactions with the imidazole ring (Fig. 1a) [23,24]. The structures of the His-RGO complex achieved after exfoliation appear nearly electron transparent in the TEM micrographs, are few μm in lateral size, and present higher image contrast features, reasonably due to folded edges and wrinkles (Fig. 1b). Also, few layers of His-RGO have been observed in the sample. UV–Vis

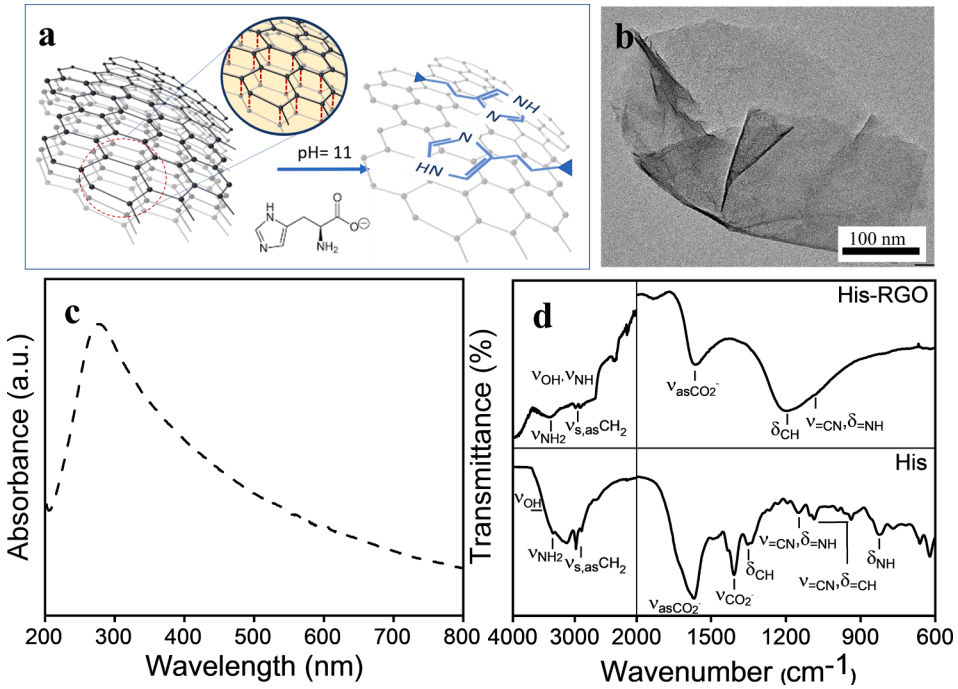

Fig. 1. (a) Sketch of the exfoliation and functionalization of RGO in His solutions at pH 11. (b) TEM micrograph of His-RGO. (c) UV–Vis absorption spectra of 0.04 mg mL^{-1} His-RGO aqueous dispersions. (d) ATR-FTIR spectra of powders of His-RGO and His, respectively from 4 mg mL^{-1} aqueous dispersions and solutions at pH 11. (The sketch is not drawn to scale).

absorption spectra of the His-RGO aqueous dispersions show an absorption peak at 275 nm, which is ascribed to the characteristic π-π* transition of the −C = C- bond of RGO (Fig. 1c), that superimposes that of His, which is expected at ca. 263 nm and reasonably ascribed to intramolecular π-π* transitions of the His imidazole ring [39], likely because of its low concentration in the His-RGO complex. Typical UV–Vis absorption features of molecular linkers functionalizing by aromatic π-π interactions the basal plane of RGO, as pyrene molecules, were observed at RGO:pyrene w/w significantly lower (1:17) [38,40] than that one used here in the preparation of the His-RGO complex, that is 1:1.6. This high w/w was purposely selected to limit the decrease of the thermal conductivity of RGO, that is induced by the organic His coating layer [41].

The successful functionalization of the RGO basal plane by His is provided by the Attenuated Total Reflection Fourier Transform Infrared (ATR-FTIR) spectra of powders of the His-RGO complex. Such infrared spectra, in fact, evidence, in the high wavenumber region, the stretching vibration of $–NH_2$ (υ_{NH2}) groups at 3394 cm^{-1}, as well as the symmetric and asymmetric stretching modes of $–CH_2$ moieties ($\upsilon_{s,asCH2}$) at 2988 cm^{-1} and 2901 cm^{-1}, respectively, observed also in the neat His (Fig. 1d). The His-RGO spectra show also the $–COO^-$ (νCOO^-) asymmetric stretching at 1564 cm^{-1} and a broad band between ca. 1380–695 cm^{-1}, originating from the overlapping of the aliphatic –CH bending (δ_{CH}), imidazole = CN stretching ($\upsilon_{=CN}$), =NH bending ($\delta_{=NH}$) and = CH bending ($\delta_{=CH}$), evident in the infrared spectrum of His at 1193 cm^{-1}, 1149 cm^{-1} and 1086 cm^{-1} [42], respectively, definitely assessing the modification of RGO with His.

Cotton (Cot) impregnation was performed by dipping in 4 mg ml^{-1} His-RGO aqueous dispersions at neutral pH. In such a condition, imidazole nitrogen atoms and carboxylate side chain groups in His are expected to favor chemisorption of His-RGO onto Cot, due to their hydrogen bond interactions (Fig. 2a) with the hydroxyl groups of the textile (Fig. S2). Cot modified by His-RGO (Cot/His-RGO) presents in its absorption spectrum the peak of RGO at 275 nm (Fig. S3).

Scanning Electron Microscopy (SEM) micrographs show the barely smooth and bright in image contrast surface morphology of the neat Cot fabrics (Fig. 2b), that significantly changes, becoming darker in the image contrast, rough, and coated by a dense layer of flakes after modification with the His-RGO sheets (Fig. 2c).

The Raman spectrum of the sample shows at 1340 cm^{-1} and 1591 cm^{-1} the typical D and G peaks, respectively of graphitic materials [43] (Fig. 2d), that are not visible in the Raman spectrum of neat Cot [44], and hence, can be ascribed to the His-RGO coating (Fig. 2d). It is worth noticing that the Raman signals of His, expected at 1320 cm^{-1} [45], are not evident in the Raman spectrum of His-RGO, because superimposed by the D mode of RGO. The strong resonant Raman signal of RGO also suppresses Raman signatures of neat Cot fabric (Fig. 2d).

3.2. Preparation of the Cot/His-RGO/Ag fabrics

Cot/His-RGO fabrics were modified with Ag NPs by dipping in 0.1 g mL^{-1} Ag precursor solutions formed of H_2O and CH_3OH at two different volume ratios, namely 9:1 v/v ($9:1_{v/v}$) and 1:1 v/v ($1:1_{v/v}$), and by exposing the wet fabrics to UV-light ($\lambda \geq 254$ nm) to induce Ag^+ photoreduction [29,30] (Fig. 3). Although methanol is an unsafe solvent, it has been used in textile industry for formulating coatings based on silicates, plant extracts and essential oils, on cellulose based substrates. This includes the production of functional and biocompatible cotton fabrics, cotton gauzes and wound dressing for biomedicine applications [46–48]. Such a procedure, in fact, has been reported in literature for the manufacture of antimicrobial commercial Cot fabrics, specifically using the Ag precursor $9:1_{v/v}$ solution [29,30].

Fig. 4 reports the SEM-EDS investigation and Raman spectrum of the Cot/His-RGO/Ag fabrics manufactured starting from the Ag precursor $1:1_{v/v}$ solution, under UV-light irradiation (Cot/His-RGO/$Ag_{1:1,UV}$). The SEM images collected by secondary electrons evidence fibers densely coated by bright microstructures (Fig. 4a, left panel), showing bright image contrast also in the same SEM image recorded by back scattered electrons (Fig. 4a, right panel). The microstructures can be mostly ascribed to Ag, as assessed by the EDS spectrum of the sample that shows its 2.984 keV Lα line (Fig. 4f), and the chemical mapping, recorded at the same Ag line, evidencing the uniform distribution of the metal onto the fabrics (Fig. 4e). Furthermore, the UV–Vis absorption spectrum of the manufactured Cot/His-RGO/Ag samples shows the typical Localized Surface Plasmon Resonance (LSPR) absorption peak of Ag NPs [49] at 360 nm (Fig. S3), thus confirming the presence of the metal nanostructures in the experimental conditions investigated. The Raman spectrum of Cot/His-RGO/$Ag_{1:1,UV}$ (Fig. 4b) exhibits the D and G peaks of RGO, that maintain the same intensity ratio and positions as in Cot/His-RGO (Fig. 2d), assessing that Raman spectroscopy does not detect the addition of structural defects to RGO in the *in situ* photoreduction of Ag^+ ions.

Ag NPs and microstructures were observed to form also after dipping the Cot/His-RGO fabrics in 0.1 g mL^{-1} Ag precursor $1:1_{v/v}$ solutions, and then letting the samples dry in dark conditions, at ambient atmosphere (Cot/His-RGO/$Ag_{1:1}$). In such experimental conditions, though electron transfers from RGO provide galvanic reduction of the Ag^+ ions [50], the Ag NPs concentration is lower than that achieved under UV-light exposure, as indicated by the lower absorption intensity of the spectrum of Cot/His-RGO/$Ag_{1:1}$ with respect to Cot/His-RGO/$Ag_{1:1,UV}$ (Fig. S3).

When the Ag precursor $9:1_{v/v}$ solution was used for impregnating Cot, and the reduction of Ag^+ was performed under UV-light irradiation, the SEM-EDS investigation of Cot/His-RGO/$Ag_{9:1,UV}$ shows uniformly distributed the bright in contrast micrometer sized structures (Fig. 5a, left panel) of Ag, appearing bright also in the SEM image collected with the signal of the back-scattered electrons (Fig. 5a, right panel). Besides, it evidences also the Lα line of Ag at 2.984 keV in the EDS spectrum (Fig. 5f), and presents the Ag, O and C elements distributed as in the chemical mapping images recorded at the Lα line of Ag (Fig. 5e), Kα line of O and at the Kα line of C (Fig. 5c-d). Also, in this sample the Raman investigation does not detect the addition of defects to the graphitic

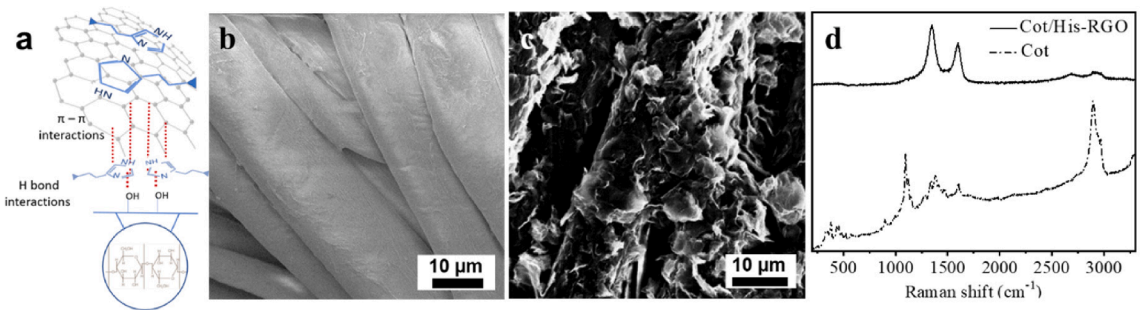

Fig. 2. (a) Sketch of the chemisorption of His-RGO onto Cot. (b-c) SEM images and (d) Raman spectra of Cot fabrics as neat (b) and impregnated by dipping into 4 $mgml^{-1}$ His-RGO aqueous dispersions (c). (The sketch is not drawn to scale).

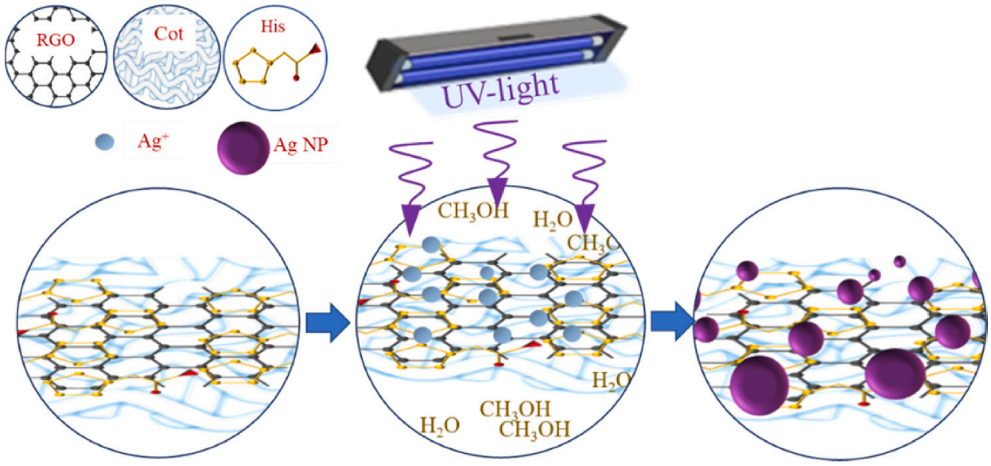

Fig. 3. Sketch of the UV-light induced photoreduction of Ag^+ ions in Ag NPs onto the Cot/His-RGO fabrics. (The sketch is not drawn to scale).

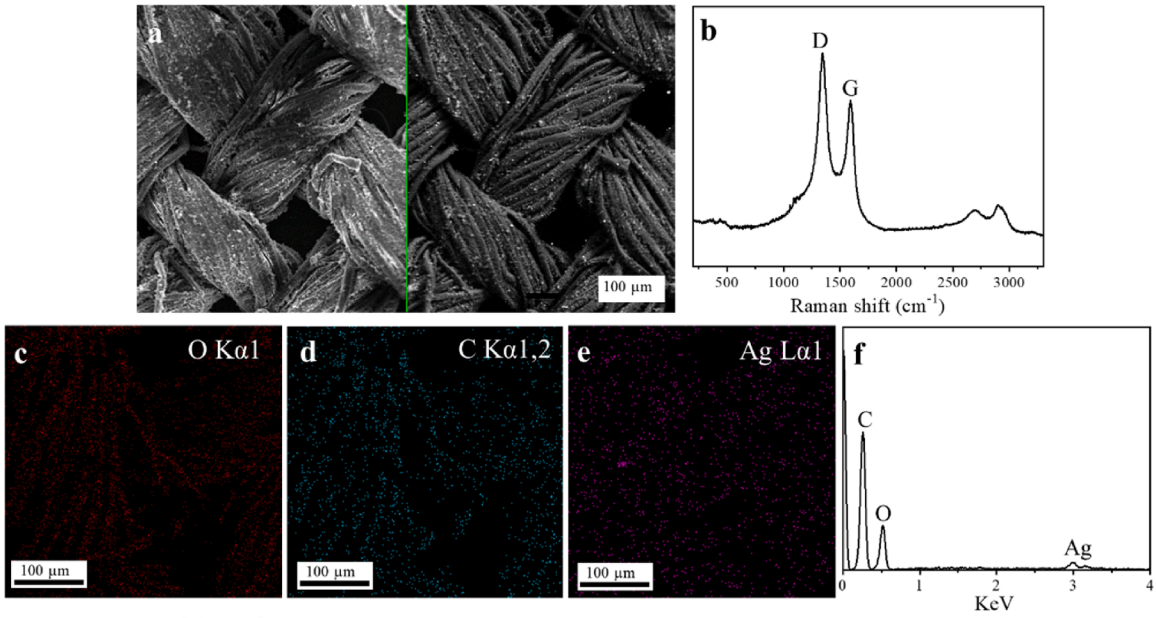

Fig. 4. (a) SEM images collected by secondary (left panel) and back scattered electrons (right panel), (b) Raman spectrum, (c-e) chemical mapping images collected at the (c) O Kα line at 0.525 eV, (d) C Kα line at 0.277 eV, and (e) Ag 2.984 keV Lα line, and (f) EDS spectrum of Cot/His-RGO/$Ag_{1:1,UV}$.

structure of RGO after the *in situ* photoreduction of the Ag^+ ions (Fig. 5b).

In Cot/His-RGO/$Ag_{9:1,UV}$, the micrometer sized Ag structures (Fig. 5a) appear larger and brighter than those obtained in Cot/His-RGO/$Ag_{1:1,UV}$ (Fig. 4a), and Ag NPs featuring a LSPR peak at 372 nm, form onto Cot, with a lower concentration with respect to that in the Cot/His-RGO/$Ag_{1:1,UV}$ samples, as assessed by the comparison of their absorbance intensities (Fig. S3).

The formation of Ag nano and microstructures can be accounted for by absorption and diffusion of Ag^+ ions into the Cot/His-RGO fabrics, induced by electrostatic and coordinating interactions between Ag^+ ions and the oxygen and nitrogen based functionalities of His-RGO, respectively, followed by heteronucleation and growth (Fig. 3). Under UV-light exposure, the reaction is expected to evolve via generation of formaldehyde from reduction of the Ag^+ ions to Ag^0 by $^{\cdot}CH_2OH$ radicals, originated the latter, from reactions between CH_3OH and $^{\cdot}OH$ radicals that form from the solvent mixture under UV-light, [51] as follow:

$$\cdot OH + CH_3OH \rightarrow -\cdot CH_2(OH) + H \quad 2O$$

$$Ag^+ + {}^{\cdot}CH_2(OH) \rightarrow Ag^0 + CH_2 = O + H^+$$

$$(Ag^0)_n + Ag^+ + {}^{\cdot}CH_2\,(OH) \rightarrow (Ag^0)_{n+1} + CH_2 = O + H^+$$

$$(Ag^0)_n + (Ag^0)_m \rightarrow (Ag^0)_{n+m}$$

XPS investigation was performed to study the surface chemistry of the Cot/His-RGO/$Ag_{1:1,UV}$ against the Cot/His-RGO and Cot/His-$RGO_{1:1,UV}$ reference samples (Fig. 6), and the same study was carried out for Cot/His-$RGO_{9:1,UV}$ and Cot/His-RGO/$Ag_{9:1,UV}$ (Fig. S4).

All the C1s spectra of Cot/His-RGO, Cot/His-$RGO_{1:1,UV}$ and Cot/His-RGO/$Ag_{1:1,UV}$ were fitted with six components (Fig. 6), specifically at 284.5 eV, 285.6 eV, 286.8 eV, 288.0 eV, 289.4 eV and 291.1 eV, that were ascribed to sp^2 C, sp^3 C, C-OH/R, C = O, C(O)OH/R and to π-π*, respectively. The contribute of His to some peaks of the C1s spectrum is expected, namely the C-N bond to the peak at 285.6 eV, while the N = C-NH group is expected to contribute to the C-OH/R peak and the carboxyl group falls underneath the peak at 289.4 eV, respectively.

The C1s spectrum of Cot/His-RGO (Fig. 6a) with its narrow and highly asymmetrical shape and the π-π* satellite peak, is typical of graphitic materials and confirm the presence of RGO at the surface of the

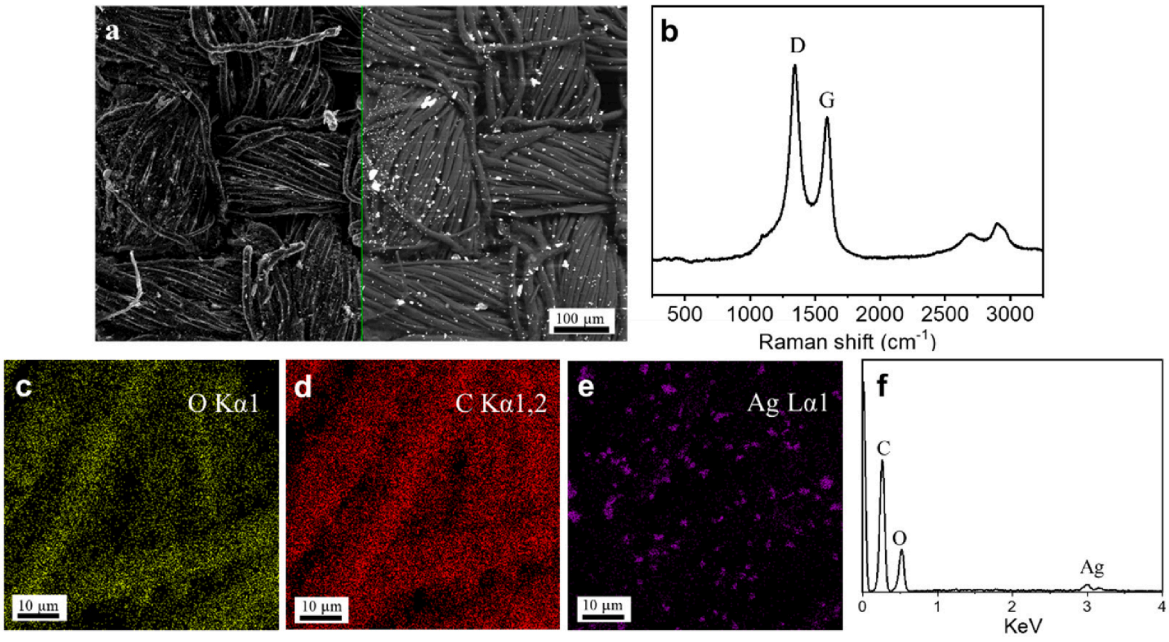

Fig. 5. (a) SEM images collected by secondary (left panel) and back scattered electrons (right panel), (b) Raman spectrum, (c-e) chemical mapping images recorded at the (c) O Kα line at 0.525 eV, (d) C Kα line at 0.277 eV and (e) Ag 2.984 keV Lα line, and (f) EDS spectrum of Cot/His-RGO/$Ag_{9:1,UV}$.

Cot fabrics. Upon impregnation with the solvent mixture (Fig. 6b) and with the Ag precursor addition (Fig. 6c), after UV-light exposure, the spectra broaden, and the high binding energy shoulder associated with oxygenated groups and sp^3 carbon increases, thus pointing out to a more functionalized RGO surface. This is confirmed by the oxygen concentration which increases from 5.5 at.% in the pristine Cot/His-RGO, up to 13.5 and 18.0 at.%, in the Cot/His-RGO$_{1:1,UV}$ and Cot/His-RGO/Ag$_{1:1,UV}$ samples, respectively.

The N1s high-resolution spectrum reported in Fig. 6d confirms the presence of His at the surface of the Cot fabrics. The N1s spectrum was curve-fitted with three peaks, namely at 399.0 eV, at lower binding energy, assigned to imidazole nitrogen (N = C-NH), at 400.0 eV ascribed to N = C-NH and the last component at 401.1 eV, due to the protonated His amine group (NH_3^+) [52]. In the N1s spectrum of the Cot/His-RGO$_{1:1,UV}$ sample, these peaks shift to lower binding energies, namely 398.5 eV, 399.6 eV and 400.9 eV, respectively (Fig. 6e). With the addition of $AgNO_3$ and heteronucleation of the Ag NPs, the imidazole nitrogen shifts to 398.8 eV (N = C-NH) and 399.2 eV (Fig. 6f), likely due to the coordination with the metal NPs and microstructures [53]. Coordination is anticipated to occur also at the $–COO^-$ functionalities of His [53]. However, the complex chemistry of the C1s component, due to overlapping signals from RGO and His, prevents distinguishing changes in the C(O)OH/R component during Ag structures formation.

The same trend in the C1s and N1s components can be observed in the XPS spectra of Cot/His-RGO$_{9:1,UV}$ and Cot/His-RGO/Ag$_{9:1,UV}$ (Fig. S4).

Moreover, the XPS investigation of the Cot/His-RGO/Ag$_{1:1,UV}$ and Cot/His-RGO/Ag$_{9:1,UV}$ samples confirms that the Ag precursor $1{:}1_{v/v}$ solutions lead to a higher atomic concentration (at.%) of Ag^+ photoreduced on the fabrics surface (Fig. 6g), and assesses, on the basis of the Ag3d high-resolution spectra, similar line shapes and peak positions of the Ag3d5/2 component at 368.4 ± 0.1 eV, indicative of metallic Ag NPs (Fig. 6h) in both samples [54], as also confirmed by the UV–Vis spectra (Fig. S3).

3.3. Thermal conductivity and surface resistivity measurements of the fabrics

Thermal conductivity (TC) of the manufactured fabrics was estimated by Differential Scanning Calorimetry (DSC) and by means of Hot Disk Thermal Constants Analyzer (TPS 2500 s), as described in Materials and methods. Typical DSC curves of neat Cot and Cot/His-RGO, which were purified from the excess of His by four ultracentrifuge washing steps, are reported in Fig. S5, and their TC are 1.1 ± 0.1 W $m^{-1}K^{-1}$ and 1.7 ± 0.2 W $m^{-1}K^{-1}$ (Fig. 7a), respectively. TC of neat Cot was also measured by using Transient Plane Source method (TPS 2500 s) obtaining a result of 0.996 ± 5 % W $m^{-1}K^{-1}$, in agreement with the value obtained by DSC.

It is worth noticing that the TC of Cot differs from the values reported in literature, which are in between 0.026–0.065 W $m^{-1}K^{-1}$ [55,56], due to the cleaning pre-treatment performed in acetone and water to remove contaminants [31]. Besides, the TC of Cot/His-RGO fabrics, which were purified from the excess of His by two ultracentrifuge steps, is lower, 1.3 ± 0.2 W $m^{-1}K^{-1}$ (Table S1, Fig. S1), than Cot/His-RGO fabrics purified by four ultracentrifuge steps (Fig. 7a), because of the excess of organic His residual from the second purification step, that decreases the thermal conduction capability of the fabrics [41].

Regarding the TC of the UV-light exposed samples, the TC of neat Cot remained constant and equal to 1.1 ± 0.1 W $m^{-1}K^{-1}$ after UV-light irradiation. In contrast, the TC of Cot/His-RGO$_{1:1,UV}$ was measured at 1.6 ± 0.1 W $m^{-1}K^{-1}$ (Fig. 7a). This value slightly increases up to 1.7 ± 0.4 W $m^{-1}K^{-1}$ in Cot/His-RGO/Ag$_{1:1}$ (Fig. 7a), and significantly enhances up to 2.1 ± 0.2 W $m^{-1}K^{-1}$ (Fig. 7a) in the Cot/His-RGO/Ag$_{1:1,UV}$ samples. The DSC curve of Cot/His-RGO/Ag$_{1:1,UV}$ is shown in Fig. S5.

The TC of Cot/His-RGO/Ag$_{1:1,UV}$ has been measured by using the Transient Plane Source method (TPS 2500 s) as well, to validate the experimental value found with DSC. In this case the TC was 1.777 ± 5 % W $m^{-1}K^{-1}$, confirming the result obtained with DSC.

For the samples prepared with the $9{:}1_{v/v}$ solutions, the TC significantly dropped to 0.9 ± 0.1 W m^{-1} K^{-1} in Cot/His-RGO$_{9:1,UV}$ (Table S1), and increased up to 1.6 ± 0.4 W m^{-1} K^{-1} in Cot/His-RGO/Ag$_{9:1,UV}$ (Table S1).

The increase of TC of the Cot/His-RGO/Ag$_{1:1,UV}$ fabrics is in line with the thermal transport capability reported for patches formed of polymer formulations based on toxic solvents, loaded with high nanofillers concentrations and fabricated by less scalable approaches [19,21].

Surface resistivity (R_s) of the modified Cot fabrics was also measured

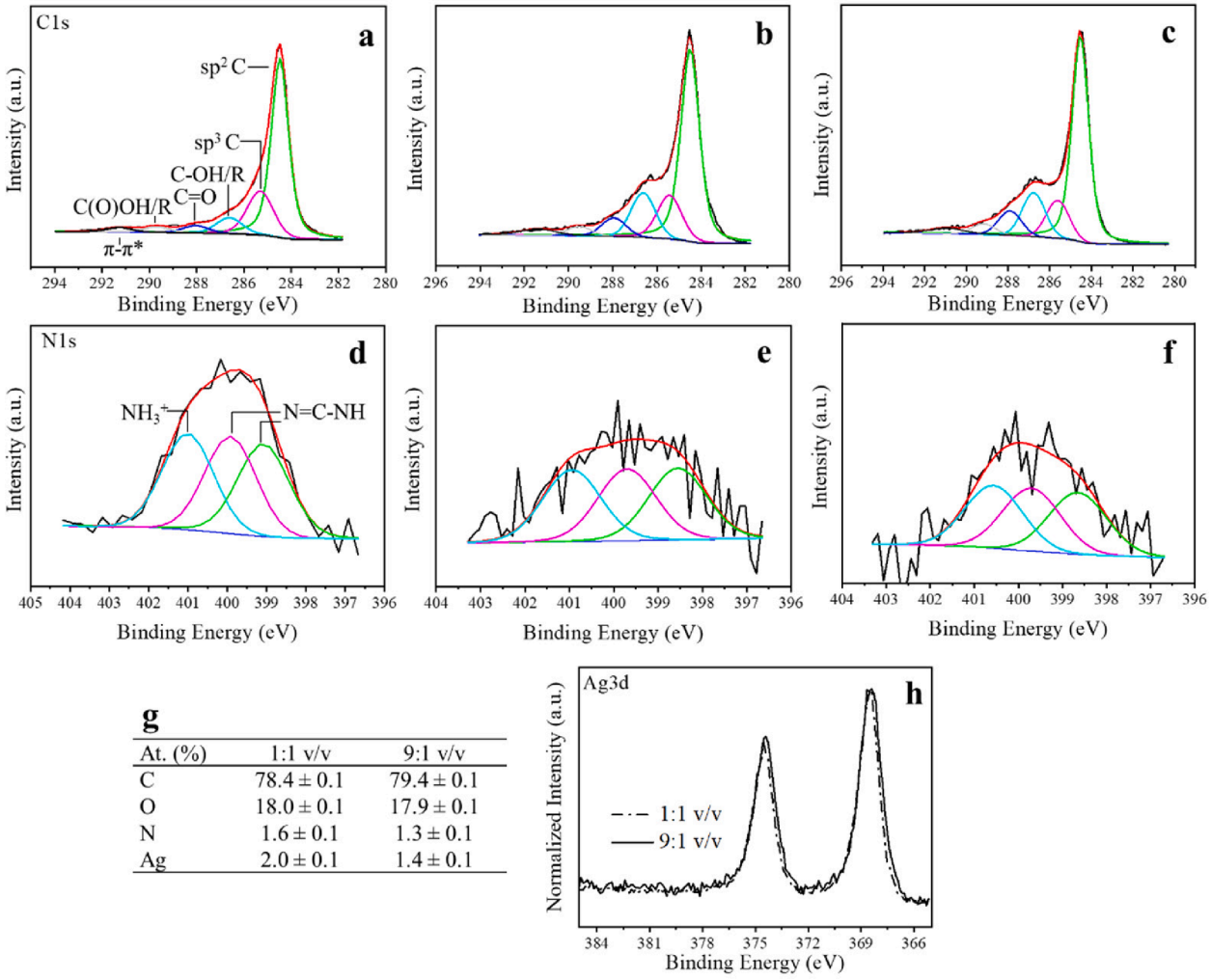

g

At. (%)	1:1 v/v	9:1 v/v
C	78.4 ± 0.1	79.4 ± 0.1
O	18.0 ± 0.1	17.9 ± 0.1
N	1.6 ± 0.1	1.3 ± 0.1
Ag	2.0 ± 0.1	1.4 ± 0.1

Fig. 6. XPS (a,b,c) C1s and (d,e,f) N1s high-resolution spectra of (a,d) Cot/His-RGO, (b,e) Cot/His-RGO$_{_1:1,UV}$ (c,f) Cot/His-RGO/Ag$_{_1:1,UV}$. (g) At.% and (h) XPS Ag3d high-resolution spectra of Cot/His-RGO/Ag$_{_1:1,UV}$ and Cot/His-RGO/Ag$_{_9:1,UV}$.

a

Sample	$AgNO_3$ (g mL^{-1})	TC (W $m^{-1}K^{-1}$) by DSC	Rs (×10^4 Ω sq^{-1})	TC (W $m^{-1}K^{-1}$) by TPS	σ (MPa)	ε (%)	E (MPa)
Cot	---	1.1 ± 0.1	---	0.996±5%	33.53 ± 1.97	22 ± 3	272.32 ± 8.97
Cot/His-RGO	---	1.7 ± 0.2	4.0	---	32.98 ± 3.06	22 ± 1	262.12 ± 23.04
Cot/His-RGO$_{_1:1,UV}$	---	1.6 ± 0.1	1.6	---	---	---	---
Cot/His-RGO/Ag$_{_1:1}$	0.01	1.7 ± 0.4	---	---	---	---	---
Cot/His-RGO/Ag$_{_1:1,UV}$	0.01	2.1 ± 0.2	1.2	1.777±5%	25.65 ± 0.90	26 ± 3	181.43 ± 9.80

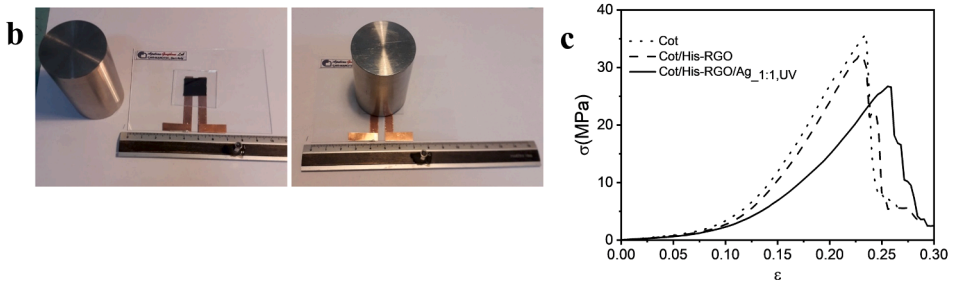

Fig.7. (a) TC of Cot, Cot/His-RGO, Cot/His-RGO$_{_1:1,UV}$, Cot/His-RGO/Ag$_{_1:1}$ and Cot/His-RGO/Ag$_{_1:1,UV}$. R_s of Cot/His-RGO, Cot/His-RGO$_{_1:1,UV}$ and Cot/His-RGO/Ag$_{_1:1,UV}$ estimated by DSC approach. TC of Cot and Cot/His-RGO/Ag$_{_1:1,UV}$ measured by TPS method. Tensile strength (σ), strain at break (ε) and tensile modulus (E) of Cot, Cot/His-RGO and Cot/His-RGO/Ag$_{_1:1,UV}$. (b) Experimental set-up for the measurement of R_s. (c) Strain-stress curves of Cot, Cot/His-RGO and Cot/His-RGO/Ag$_{_1:1,UV}$.

according to the method reported in [36] (Fig. 7b), as described in Materials and methods.

R_s of the Cot/His-RGO fabrics is ca. 4.0×10^4 Ω sq^{-1} and it decreases in Cot/His-RGO$_{1:1,UV}$ and Cot/His-RGO/Ag$_{1:1,UV}$ down to 1.6×10^4 Ω sq^{-1} and 1.2×10^4 Ω sq^{-1} (Fig. 7a), respectively. On the contrary, Cot/His-RGO$_{9:1,UV}$ and Cot/His-RGO/Ag$_{9:1,UV}$ have a R_s slightly lower, namely 1.3×10^4 Ω sq^{-1} and 1.0×10^4 Ω sq^{-1}, respectively (Table S1).

It is worthwhile considering that, a noticeable increase of thermal conductivity was accomplished, although the C/O ratio of the Cot/His-RGO/Ag$_{1:1,UV}$ sample is ca. 2 (Table S2), attesting its low conductivity, which is likely due to the high density of oxygen based functionalities of the immobilized His molecules necessary [57], however, to process RGO from aqueous dispersions for modifying cotton by impregnation.

A plausible explanation for the observed trends in TC and Rs is the interplay between i. the formation of $^{\cdot}CH_2OH$ species from reaction of $^{\cdot}OH$ radicals, which generate from water under UV-light irradiation, and CH_3OH, that lead to the formation of Ag NPs filling the gaps among the His-RGO sheets, and hence increasing both TC and reducing R_s [58] (Fig. 7a), and ii. the reaction of $^{\cdot}OH$ radicals with RGO that grafts −C-OH and −C = O groups onto its basal plane, as assessed by XPS analyses (Fig. 6b,c, Fig. S4b,c) [58,59], leading to a p-doping effect of His-RGO that decreases R_s [59] and concomitantly provides phonon scattering phenomena that reduce TC [60]. These hypotheses can reasonably explain the evidence that for the Cot/His-RGO/Ag$_{1:1,UV}$ fabrics, which were achieved under UV-light exposure from the Ag precursor $1{:}1_{v/v}$ solution, in which the photogenerated $^{\cdot}OH$ radicals could be scavenged mostly by methanol, instead of reacting with RGO, leading to $^{\cdot}CH_2OH$ species favoring formation of Ag NPs in a larger concentration (Fig. S3), higher TC and R_s were observed (Fig. 7a).

3.4. Atomic force Microscopy (AFM) investigation of the fabrics

In order to go in depth into the factors that lead to the observed increase of TC in the Cot/His-RGO/Ag$_{1:1,UV}$ fabric samples, their surface morphology was investigated by AFM and compared to that of neat cotton, to achieve information concerning quality and effectiveness of the applied coating. The AFM phase imaging, combined with topography, is particularly suited for such a purpose, as given that AFM phase imaging is capable of sensing variations in stiffness, it is possible to distinguish between parts of the surface that are exposed, from those that are fully covered with the nanocomposite [61].

Fig. 8 reports the AFM height images of the cotton fibers, before and after applying the His-RGO/Ag$_{1:1,UV}$ coating, as well as the corresponding AFM phase images. The topography images of the uncoated sample show irregularities of the cotton fibers (Fig. 8a), that are confirmed by phase images (Fig. 8b), whereas the absence of cracks in both the topography and phase images of the Cot/His-RGO/Ag$_{1:1,UV}$ samples (Fig. 8c-d) is an indication of the uniform surface coverage of the textile, thus explaining its good thermal conductivity values. In addition, the height profile recorded along lines of the topography image of the Cot/His-RGO/Ag$_{1:1,UV}$ sample (Fig. 8e) shows the formation of Ag NPs having size of tens nm. Finally, surface roughness measurements were determined by evaluating the root mean square roughness (Rq) values of the investigated areas. The measured Rq values are 47.2 nm and 14.2 nm, respectively for the neat Cot and the Cot/His-RGO/Ag$_{1:1,UV}$ fabric samples, confirming the presence of a smooth and continuous nanocomposite coating.

3.5. Mechanical properties, water contact angle analyses, oxygen permeability and durability of fabrics

Tensile tests were performed to investigate the effect of the coating of Cot with His-RGO and His-RGO/Ag$_{1:1,UV}$ on its mechanical properties. The results show that the mean values estimated for strength (σ) and strain at break (ε) do not statistically differ in Cot and Cot/His-RGO samples (Fig. 7a), while a slight decreases of the tensile modulus (E) with the treatment with His-RGO was noticed (Fig. 7a). After treatment with His-RGO/Ag$_{1:1,UV}$, the mean value of σ decreases of ca. 20 %, as well as E, which decreases of ca. 33 %, while ε increases of 13 % (Fig. 7a). These results assess that the nanocomposite coating treatment enhances the intrinsic flexibility of Cot, letting to infer an improvement in wear comfort [62], moderately reducing its tensile strength, evidence that could be likely be due to the local heating of the fabric generated under UV-light irradiation [63].

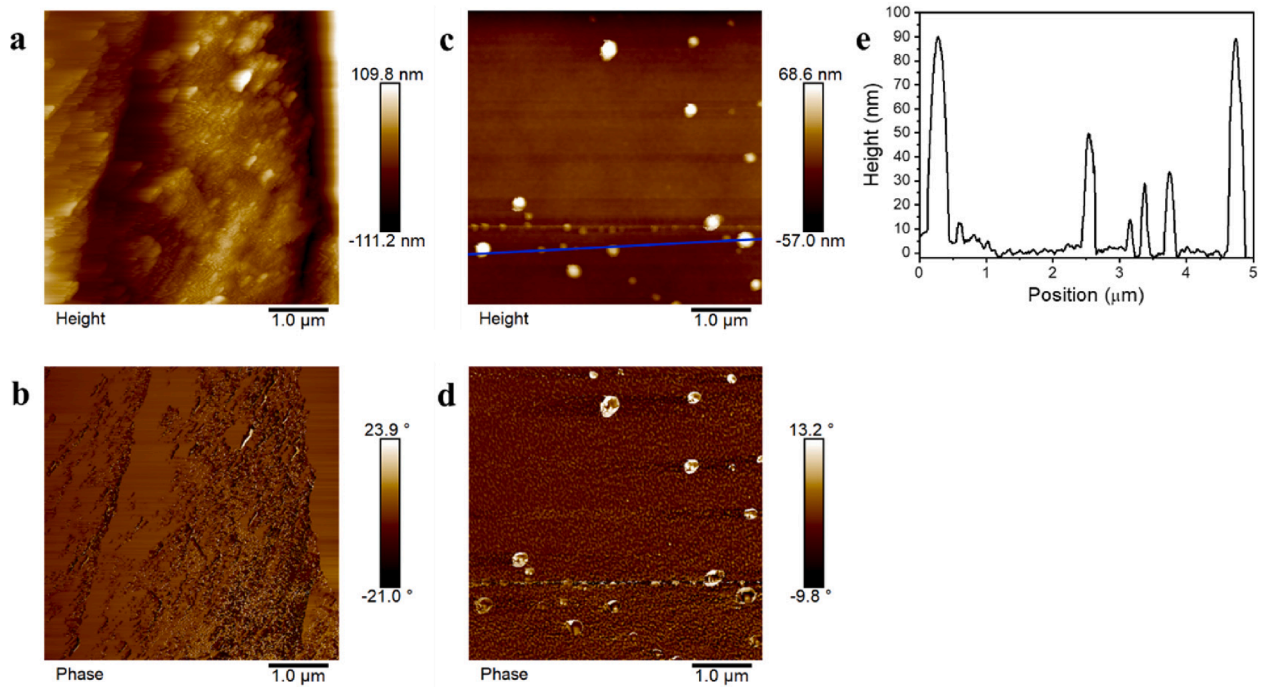

Fig. 8. (a,c) Tapping- and (b,d) phase-mode 2D-view AFM images of the (a,b) Cot and (c,d) Cot/His-RGO/Ag$_{1:1,UV}$ samples. In (e) cross sectional profile taken along the blue line marked in (c). (For interpretation of the references to colour in this figure legend, the reader is referred to the web version of this article.)

Besides, oxygen permeability tests of the Cot/His-RGO/Ag$_{1:1,UV}$ fabric samples showed that the coating does not modify the breathability of the textiles (data not shown), likely because it preserves the spaces among the yarns of the fabric texture [64], as also assessed by the SEM images (Fig. 4a and Fig. 5a).

Cot is characterized by a very fast absorption of water due to capillary effects requiring long times and high energy consumption for its drying, and hence, additional finishes are often used to convey hydrophobicity properties [65]. In this regard, water absorption behaviour of the fabrics was investigated by contact angle (WCA) measurements, and while bare Cot absorbs water, Cot/His-RGO/Ag$_{1:1,UV}$ presents a lower absorption capability with WCA of 100 ± 10, likely due to the increased roughness of the coating [66] and to the moisture barrier and hydrophobic properties of RGO [67].

The washing durability of the His-RGO/Ag$_{1:1,UV}$ coating was investigated by monitoring the mean values of TC and static WCA after 5, 10 and 20 laundering cycles (Fig. 9). As it can be noticed, the washing durability is low, in fact, the TC of Cot/ His-RGO/Ag$_{1:1,UV}$ reaches almost the same values as the Cot/His-RGO sample, passing from 2.1 ± 0.2 W m^{-1} K^{-1}, to 2.0 ± 0.1 W m^{-1} K^{-1} after 5 cycles, 1.9 ± 0.1 W m^{-1} K^{-1} after 10 cycles and 1.6 ± 0.2 W m^{-1} K^{-1} after 20 cycles. Concomitantly, the WCA decreases from 100 ± 10, to 74 ± 2, 64 ± 3 and to 31 ± 2, assessing a reduction of the hydrophobicity of ca. 70 %. Therefore, further investigation is necessary to overcome this limitation, for instance by means of the use of a self-polymerizable and flexible biocompatible polymer coating as polydopamine, a 'molecular glue', [68] able to sustain the alkaline washing environment of detergents and acting as an adhesive of the nanocomposite onto the textile.

4. Conclusions

A new thermally conductive hybrid nanocomposite coating for cotton (Cot), formed by histidine functionalized Reduced Graphene Oxide (His-RGO), decorated with tens nm in size Ag nanoparticles (NPs) and microstructures, was manufactured by an ecofriendly, scalable, and sustainable approach. The strategy consisted of impregnating Cot by dipping in His-RGO aqueous dispersions, and then, in $AgNO_3$ solutions, 1:1 v/v in H_2O:CH_3OH, followed by UV-light irradiation, in air, inducing the *in situ* photoreduction of the Ag NPs onto the textile from $AgNO_3$. His was selected because of its biocompatibility, water solubility, and capability to bind RGO by aromatic π-π stacking interactions allowing its dispersion in water, and concomitantly, coordinate the Ag NPs, also favoring chemisorption of the His-RGO coating to Cot by hydrogen interactions. Thermal conductivity of the nanocomposite modified Cot fabrics was measured by DSC and was validated by TPS method. The preliminary results are promising, as thermal conductivity of the coating is found twice that of the neat Cot, due to the bare components' contribution to the resulting textile thermal transport capability, and to the establishment of more extended heat conduction percolation paths among the photogenerated Ag NPs and the His-RGO sheets. The thermal transport capability of the manufactured coating is, indeed, in line with those reported in literature for patches fabricated by expensive technologies, formed of polymer formulations heavily loaded by high thermally conductive nanofillers and that use, in some works, also toxic solvents, that, in fact, result in less sustainable and scalable methodologies. Besides, effectiveness of the DSC technique in measuring thermal conductivity of fabrics is here assessed. The nanocomposite coating preserves oxygen permeability and increases flexibility of Cot, letting to infer an improvement in wear comfort, while only moderately reducing its strength, and decreases its water absorption capability. The next steps should focus on improving the adhesion of the nanocomposite coating to cotton, and ensuring its durability through washing, particularly under the alkaline conditions of detergents. The reported preliminary study of the coating makes it promising for the development of natural IR-opaque passive cooling textiles, and further investigation is necessary for assessing textile's radiative heat dissipation capability and thermal comfort properties.

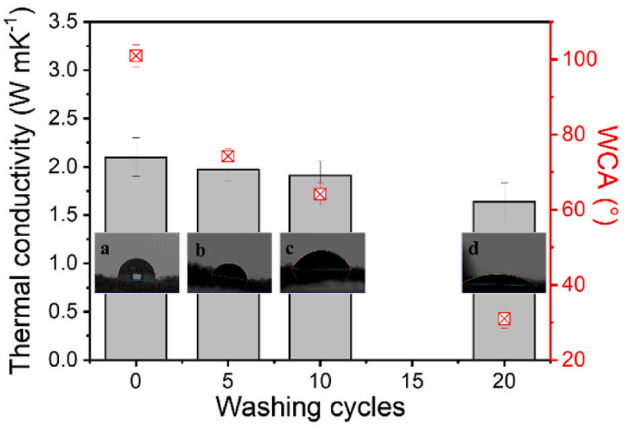

Fig. 9. TC and WCA values of the Cot/His-RGO/Ag$_{1:1,UV}$ sample, as prepared and after 5, 10 and 20 washing cycles. (In the insets) Water droplet image on Cot/His-RGO/Ag$_{1:1,UV}$ before (a) and after 5 (b), 10 (c) and 20 (d) washing cycles.

CRediT authorship contribution statement

Giacomo Mandriota: Methodology, Investigation, Funding acquisition. **Adriana Grandolfo:** Methodology, Investigation, Data curation. **Raffaella Striani:** Methodology, Investigation, Data curation. **Annamaria Panniello:** Methodology, Investigation, Data curation. **Giuseppe V. Bianco:** Methodology, Investigation, Conceptualization, Data curation. **Antonella Milella:** Methodology, Investigation. **Claudio Mele:** Writing – original draft, Methodology, Investigation, Data curation, Conceptualization. **Roberto Comparelli:** Resources, Funding acquisition. **Antonio Greco:** Funding acquisition, Data curation, Conceptualization. **Marinella Striccoli:** Funding acquisition. **Elisabetta Fanizza:** Resources. **Gianpiero Colangelo:** Conceptualization, Data curation, Methodology, Validation. **M. Lucia Curri:** Conceptualization, Writing-review & editing. **Chiara Ingrosso:** Writing – review & editing, Writing – original draft, Supervision, Resources, Project administration, Methodology, Investigation, Funding acquisition, Data curation, Conceptualization. **Carola Esposito Corcione:** Writing – review & editing, Writing – original draft, Supervision, Resources, Project administration, Methodology, Investigation, Funding acquisition, Data curation, Conceptualization.

Declaration of competing interest

The authors declare that they have no known competing financial interests or personal relationships that could have appeared to influence the work reported in this paper.

Acknowledgments

The authors wish to thank the Italian National Institute for Insurance against Accidents at Work (INAIL) (Italy) (www.inail.it) for its financial support of the project TRANSISTOR "Tessuti in nanocompositi a base di gRAfene e seNsori wireleSs Indossabili a SupporTo del cOmfort teRmico" through the fund "Bando BRiC. Bando Ricerche in Collaborazione (BRiC – 2019)" and Italian PON MIUR funded project PON ECOTEC (ARS0_00951).

Appendix A. Supplementary data

Supplementary data to this article can be found online at https://doi.org/10.1016/j.apsusc.2024.161884.

Data availability

Data will be made available on request.

References

[1] Y. Zhang, X. Xia, K. Ma, G. Xia, M. Wu, Y.H. Cheung, H. Yu, B. Zou, X. Zhang, O. K. Farha, J.H. Xin, Functional Textiles with Smart Properties: Their Fabrications and Sustainable Applications, Adv. Funct. Mater. 33 (2023) 2301607, https://doi.org/10.1002/adfm.202301607.

[2] G. Li, F. Sun, S. Zhao, R. Xu, H. Wang, L. Qu, M. Tian, Autonomous Electroluminescent Textile for Visual Interaction and Environmental Warning, Nano Lett. 23 (2023) 8436–8444, https://doi.org/10.1021/acs.nanolett.3c01653.

[3] M. Li, Z. Li, L. Qu, F. Chen, M. Tian, Recent Progress of the Active Materials with Various Micro-structures for Flexible Textile-Based Supercapacitors for Flexible, Adv. Fiber Mater. 4 (2022) 1005–1026, https://doi.org/10.1007/s42765-022-00166-3.

[4] R. Xu, M. She, J. Liu, S. Zhao, H. Liu, L. Qu, M. Tian, Breathable Kirigami-Shaped Ionotronic e-Textile with Touch/Strain Sensing for Friendly Epidermal Electronics, Adv. Fiber Mater. 4 (2022) 525–1534, https://doi.org/10.1007/s42765-022-00186-z.

[5] C. Ingrosso, A. Petrella, M.L. Curri, M. Striccoli, P. Cosma, P.D. Cozzoli, A. Agostiano, Photoelectrochemical properties of Zn(II) phthalocyanine/ZnO nanocrystals heterojunctions: Nanocrystal surface chemistry effect, Appl. Surf. Sci. 246 (2005) 367–371, https://doi.org/10.1016/j.apsusc.2004.11.041.

[6] M.L. Curri, R. Comparelli, M. Striccoli, A. Agostiano, Emerging methods for fabricating functional structures by patterning and assembling engineered nanocrystals, Phys. Chem. Chem. Phys. 12 (2010) 11197–11207, https://doi.org/10.1039/B926146J.

[7] H. Yu, S. Zhang, Y. Lian, M. Liu, M. Wang, J. Jiang, C. Yang, S. Jia, M. Wu, Y. Liao, J. Gou, Y. Jiang, J. Wang, G. Tao, Electronic Textile with Passive Thermal Management for Outdoor Health Monitoring, Adv. Fiber Mater. 6 (2024) 1241–1252, https://doi.org/10.1007/s42765-024-00412-w.

[8] J. Wang, Q. Li, D. Liu, C. Chen, Z. Chen, J. Ha, Y. Li, J. Zhang, M. Naebe, W. Lei, High temperature thermally conductive nanocomposite textile by "green" electrospinning, Nanoscale 10 (2018) 16868, https://doi.org/10.1039/C8NR05167D.

[9] Y. Peng, Y. Cui, Advanced Textiles for Personal Thermal Management and Energy, Joule 4 (2020) 724–742, https://doi.org/10.1016/j.joule.2020.02.011.

[10] X. Lan, Y. Wang, J. Peng, Y. Si, J. Ren, B. Ding, B. Li, Designing heat transfer pathways for advanced thermoregulatory textiles, Mater. Today Phys. 17 (2021) 100342–100370, https://doi.org/10.1016/j.mtphys.2021.100342.

[11] M.J. Rahman, T. Mieno, Conductive Cotton Textile from Safely Functionalized Carbon Nanotubes, J. Nanomater. 10 (2015) 978484, https://doi.org/10.1155/2015/978484.

[12] H. Zhou, H. Wang, H. Niu, C. Zeng, Y. Zhao, Z. Xu, S. Fu, T. Lin, One-Way Water-Transport Cotton Fabrics with Enhanced Cooling Effect, Adv. Mater. Interfaces 3 (2016) 1600283, https://doi.org/10.1002/admi.201600283.

[13] A. Abbas, Y. Zhao, X. Wang, T. Lin, Cooling effect of MWCNT-containing composite coatings on cotton fabrics, J. Text. I (104) (2013) 798–807, https://doi.org/10.1080/00405000.2012.757007.

[14] A. Abbas, Y. Zhao, J. Zhou, X. Wang, T. Lin, Improving Thermal Conductivity of Cotton Fabrics Using Composite Coatings Containing Graphene, Multiwall Carbon Nanotube or Boron Nitride Fine Particles, Fibers and Polym. 14 (2013) 1641–1649, https://doi.org/10.1007/s12221-013-1641-y.

[15] M. Dai, Y. Zhai, Y. Zhang, A green approach to preparing hydrophobic, electrically conductive textiles based on waterborne polyurethane for electromagnetic interference shielding with low reflectivity, Chem. Eng. J. 421 (2021) 127749–127759, https://doi.org/10.1016/j.cej.2020.127749.

[16] Y. Wang, W. Wang, R. Xu, Z. Meifang, D. Yu, Flexible, durable and thermal conducting thiol-modified RGO-WPU/cotton fabric for robust electromagnetic interference shielding, Chem. Eng. J. 360 (2019) 817–828, https://doi.org/10.1016/j.cej.2018.12.045.

[17] Y.C. Soong, C.W. Chiu, Multilayered graphene/boron nitride/thermoplastic polyurethane composite films with high thermal conductivity, stretchability, and washability for adjustable-cooling smart clothes, J. Colloid Interface Sci. 599 (2021) 611–619, https://doi.org/10.1016/j.jcis.2021.04.123.

[18] R.J. Slocombe, E.E. Hardy, J.H. Saunders, R.L. Jenkins, Phosgene Derivatives. The Preparation of Isocyanates, Carbamyl Chlorides and Cyanuric Acid1, J. Am. Chem. Soc. 72 (1950) 1888–1891, https://doi.org/10.1021/ja01161a009.

[19] T. Gao, Z. Yang, C. Chen, Y. Li, K. Fu, J. Dai, E.M. Hitz, H. Xie, B. Liu, J. Song, B. Yang, L. Hu, Three-Dimensional Printed Thermal Regulation Textile, ACS Nano 11 (2017) 11513–11520, https://doi.org/10.1021/acsnano.7b06295.

[20] K. Wu, L. Yu, C. Lei, J. Huang, D. Liu, Y. Liu, Y. Xie, F. Chen, Q. Fu, Green Production of Regenerated Cellulose/Boron Nitride Nanosheet Textiles for Static and Dynamic Personal Cooling, ACS Appl. Mater. Interfaces 11 (2019) 40685–40693, https://doi.org/10.1021/acsami.9b15612.

[21] J. Xi, X. Kong, L. Li, Z. Zhang, Y. Chen, M. Li, Y. Qin, T. Cai, W. Dai, S. Fang, J. Yi, C.-T. Lin, K. Nishimura, N. Jiang, J. Yu, High Thermal Conductivity and Radiative Cooling Designed Boron Nitride Nanosheets/Silk Fibroin Films for Personal Thermal Management, ACS Appl. Mater. Interfaces 16 (2024) 7732–7741, https://doi.org/10.1021/acsami.3c16602.

[22] T.Y. Kim, C.-H. Park, N. Marzari, The Electronic Thermal Conductivity of Graphene, Nano Lett. 16 (2016) 2439–2443, https://doi.org/10.1021/acs.nanolett.5b05288.

[23] S. Elumalai, S.B. Jaber, S. Chandrasekaran, M. Ogawa, An experimental and steered molecular dynamics simulation approach to histidine assisted liquid-phase exfoliation of graphite into few-layer graphene, Phys. Chem. Chem. Phys. 22 (2020) 9910–9914, https://doi.org/10.1039/D0CP01033B.

[24] L. Zhang, Y. Sheng, A. Z. Yazdi, K. Sarikhani, F. ang, Y. Jiang, J.Liu, T. Zheng, W. Wang, P. Ouyang, P. Chen, Surface-assisted assembly of a histidine-rich lipidated peptide for simultaneous exfoliation of graphite and functionalization of graphene nanosheets, Nanoscale 11 (2019) 2999 – 3012, doi:10.1039/C8NR08397E.

[25] Z.G. Fthenakis, Z. Zhu, D. Tománek, Effect of structural defects on the thermal conductivity of graphene: From point to line defects to haeckelites, PhysRevB 89 (2014) 125421–125426, https://doi.org/10.1103/PhysRevB.89.125421.

[26] C. Ingrosso, V. Valenzano, M. Corricelli, A. Testolin, V. Pifferi, G.V. Bianco, R. Comparelli, N. Depalo, E. Fanizza, M. Striccoli, A. Agostiano, I. Palchetti, L. Falciola, M.L. Curri, PbS Nanocrystals Decorated Reduced Graphene Oxide for NIR Responsive Capacitive Cathodes, Carbon 182 (2021) 57–69, https://doi.org/10.1016/j.carbon.2021.05.040.

[27] M. Rycenga, C.M. Cobley, J. Zeng, W. Li, C.H. Moran, Q. Zhang, D. Qin, Y. Xia, Controlling the synthesis and assembly of silver nanostructures for plasmonic applications, Chem. Rev. 111 (2011) 3669–3712, https://doi.org/10.1021/cr100275d.

[28] Y. Li, X. Li, M.M. Alam, D. Yu, M. Miao, P. Cao, R. Chen, B. Xia, Q.Q. Wu, Incorporating Ag Nanowires into Graphene Nanosheets for Enhanced Thermal Conductivity: Implications for Thermal Management, ACS Appl, Nano Mater 3 (2020) 6061–6070, https://doi.org/10.1021/acsanm.0c01265.

[29] M. Rehan, A. Barhoum, G.V. Assche, A. Dufresne, L. Gatjen, R. Wilken, Towards multifunctional cellulosic fabric: UV photo-reduction and in-situ synthesis of silver nanoparticles into cellulose fabrics, Int. J. Biol. Macromol. 98 (2017) 877–886, https://doi.org/10.1016/j.ijbiomac.2017.02.058.

[30] F. Paladini, S. De Simone, A. Sannino, M. Pollini, Antibacterial and Antifungal Dressings Obtained by Photochemical Deposition of Silver Nanoparticles, J. Appl. Polym. Sci. 131 (2014) 40326–40334, https://doi.org/10.1002/app.40326.

[31] M. Merzlyakov, C. Schick, Thermal conductivity from dynamic response of DSC, Thermochim. Acta 377 (2001) 183–191, https://doi.org/10.1016/S0040-6031(01)00553-6.

[32] S.M. Marcus, R. Blaine, Thermal conductivity of polymers, glasses and ceramics by modulated DSC, Thermochim. Acta 243 (1994) 231–239, https://doi.org/10.1016/0040-6031(94)85058-5.

[33] S. Bhattacharjee, C. R.Macintyre, X. Wen, P. Bahl, U. kumar, A. A. Chughtai, R. Joshi, Nanoparticles incorporated graphene-based durable cotton fabrics, Carbon 166 (2020) 149-163, doi:10.1016/j.carbon.2020.05.029.

[34] J.H. Flynn, D.M. Levin, A method for the determination of thermal conductivity of sheet materials by differential scanning calorimetry (DSC), Thermochim. Acta 126 (1988) 93–100, https://doi.org/10.1016/0040-6031(88)87254-X.

[35] Normal Protocol 33/89, Contact Angle Determinations (1993).

[36] AATCC TECHNICAL MANUAL, Vol.85, pag.97, Copyright © 2009 American Association of Textile Chemists and Colorists, www.aatcc.org.

[37] Food and Nutritional Components in Focus, Imidazole Dipeptides: Chemistry, Analysis, Function and Effects, Edited by Victor R Preedy, RSC, London, 2015.

[38] C. Ingrosso, M. Corricelli, A. Disha, E. Fanizza, G.V. Bianco, N. Depalo, A. Panniello, A. Agostiano, M. Striccoli, M.L. Curri, Solvent dispersible nanocomposite based on Reduced Graphene Oxide in situ decorated with gold nanoparticles, Carbon 152 (2019) 777–787, https://doi.org/10.1016/j.carbon.2019.06.070.

[39] E. Satheeshkumar, A. Bandyopadhyay, M.B. Sreedhara, S.K. Pati, C.N.R. Rao, M. Yoshimura, One-Step Simultaneous Exfoliation and Covalent Functionalization of MoS_2 by Amino Acid Induced Solution Processes, ChemNanoMat 3 (2017) 172–177, https://doi.org/10.1002/cnma.201600363.

[40] C. Ingrosso, F. Bettazzi, M. Corricelli, A. Testolin, V. Pifferi, G.V. Bianco, N. Depalo, E. Fanizza, M.L. Curri, M. Striccoli, I. Palchetti, L. Falciola, Au nanoparticle decorated reduced graphene oxide and its electroanalytical characterization for label free dopamine detection, Mater. Adv. 5 (2024) 549–560, https://doi.org/10.1039/d3ma00785e.

[41] K. C. Chan, C. Y. Tso, A. Hussain, Christopher Y.H. Chao, A theoretical model for the effective thermal conductivity of graphene coated metal foams, Appl. Therm. Eng. 161 (2019) 11411, doi:10.1016/j.applthermaleng.2019.114112.

[42] J.G. Mesu, T. Visser, F. Soulimani, B.M. Weckhuysen, Infrared and Raman spectroscopic study of pH-induced structural changes of L-histidine in aqueous environment, Vib. Spectrosc. 39 (2005) 114–125, https://doi.org/10.1016/j.vibspec.2005.01.003.

[43] A.C. Ferrari, J. Robertson, Interpretation of Raman spectra of disordered and amorphous carbon, J. Phys. Rev. B 61 (2000) 14095–14107, https://doi.org/10.1103/PhysRevB.61.14095.

[44] D. Puchowicz, M. Cieslak, Raman Spectroscopy in the Analysis of Textile Structures, in: C. S. Pathak, S. Kumar (Eds) Recent, Developments in Atomic Force Microscopy and Raman Spectroscopy for Materials Characterization, IntechOpen, 2021, doi:10.5772/intechopen.99731.

[45] G. Zhu, X. Zhu, Q. Fan, X. Wan, Raman spectra of amino acids and their aqueous solutions, Spectrochim. Acta A 78 (2011) 1187–1195, https://doi.org/10.1016/j.saa.2010.12.079.

[46] M. Rehan, M. El-Shahat, A.S. Montaser, R.M. Abdelhameed, Functionalization strategy of carboxymethyl cotton gauze fabrics with zeolitic imidazolate framework-67 (ZIF-67) as a recyclable material for biomedical applications,

Internat. J. Biol. Macromol. 279 (2024) 135148, https://doi.org/10.1016/j.ijbiomac.2024.135148.
[47] H.E. Emam, O.M. Darwesh, R.M. Abdelhameed, Protective Cotton Textiles via Amalgamation of Cross-Linked Zeolitic Imidazole Frameworks, Ind. Eng. Chem. Res. 59 (2020) 10931–10944, https://doi.org/10.1021/acs.iecr.0c01384.
[48] A. Rehman, A. Ahmad, A. Hameed, S. Kiran, T. Farooq, Green dyeing of modified cotton fabric with Acalypha wilkesiana leave extracts, Sust. Chem. Pharm. 21 (2021) 100432, https://doi.org/10.1016/j.scp.2021.100432.
[49] K.C. Lee, S.J. Lin, C.H. Lin, C.S. Tsai, Y.J. Lu, Size effect of Ag nanoparticles on surface plasmon resonance, Surf. Coat. Technol. 202 (2008) 5339–5342, https://doi.org/10.1016/j.surfcoat.2008.06.080.
[50] Y. Park, J.Y. Koo, S. Kim, H.C. Choi, Spontaneous Formation of Gold Nanoparticles on Graphene by Galvanic Reaction through Graphene, ACS Omega 4 (2019) 18423–18427, https://doi.org/10.1021/acsomega.9b02691.
[51] K. Chandrasekaran, J.K. Thomas, The mechanism of the photochemical oxidation of water to oxygen with silver chloride colloids, Chem. Phys. Lett. 97 (1983) 357–360, https://doi.org/10.1016/0009-2614(83)80507-7.
[52] O. Kostko, B. Xu, M. Ahmed, Local electronic structure of histidine in aqueous solution, Phys. Chem. Chem. Phys. 23 (2021) 8847–8853, https://doi.org/10.1039/D1CP00361E.
[53] P. Budurua, B.C.S.R. Reddy, N.V.S. Naidua, Functionalization of silver nanoparticles with glutamine and histidine for simple and selective detection of Hg^{2+} ion in water samples, Sens. & Actuators B: Chem. 244 (2017) 972–982, https://doi.org/10.1016/j.snb.2017.01.041.
[54] I. Lopez-Salido, D.C. Lim, Y.D. Kim, Ag nanoparticles on highly ordered pyrolytic graphite (HOPG) surfaces studied using STM and XPS, Surf. Sci. 588 (2005) 6–18, https://doi.org/10.1016/j.susc.2005.05.021.
[55] P. J. Rivero, Aitor Urrutia, J. Goicoechea, F. J. Arregui, The thermal conductivity of textiles, Nanoscale Res. Lett. 10 (2015) 501, doi:10.1088/0959-5309/58/1/310.
[56] O.I. Kalaoglu-Altan, B.K. Kayaoglu, L. Trabzon, Improving Thermal Conductivities of Textile Materials by Nanohybrid Approaches 103825 (2022) doi:10.1016/j.isci.2022.103825 iScience 25.
[57] O.C. Compton, B. Jain, D.A. Dikin, A. Abouimrane, K. Amine, S.B.T. Nguyen, ACS Nano 5 (2011) 4380–4391, https://doi.org/10.1021/nn1030725.
[58] E.J. Radich, P.V. Kamat, Making graphene holey gold-nanoparticle-mediated hydroxyl radical attack on reduced graphene oxide, ACS Nano 7 (2013) 5546–5557, https://doi.org/10.1021/nn401794k.
[59] R. Singla, A. Kottantharayil, Stable hydroxyl functionalization and p-type doping of graphene by a non-destructive photo-chemical method, Carbon 152 (2019) 267–273, https://doi.org/10.1016/j.carbon.2019.06.021.
[60] S. Mann, I. Mudahar, H. Sharma, V.K. Jindal, G.S. Dubey, G. Gumbs, V. Fessatidis, Lattice thermal conductivity of pure and doped (B, N) Graphene, Mater. Res. Express 7 (2020) 095003, https://doi.org/10.1088/2053-1591/abb2cd.
[61] A.I.S. Neves, D.P. Rodrigues, A. De Sanctis, E. Torres Alonso, M.S. Pereira, V. S. Amaral, L.V. Melo, S. Russo, I. de Schrijver, H. Alves, M.F. Craciun, Towards conductive textiles: coating polymeric fibres with graphene, Scientific Reports 7 (2017) 1–10, https://doi.org/10.1038/s41598-017-04453-7.
[62] H. Jun Sim, H. Gwac, S. J. Kim, J.-M. Oh, C. Choi, Soft and elastic hygroelectric fiber for wearable human monitoring textiles, Chem. Eng. J. 495 (2024) 153486, doi:10.1016/j.cej.2024.153486.
[63] L. Guardia, S. Villar-Rodil, J.I. Paredes, R. Rozada, A. Martınez-Alonso, J.M. D. Tascon, UV light exposure of aqueous graphene oxide suspensions to promote their direct reduction, formation of graphene–metal nanoparticle hybrids and dye degradation, Carbon 50 (2012) 1014–1024, https://doi.org/10.1016/j.carbon.2011.10.005.
[64] M.G. Chakroun, M.G. Chakroun, S. Benltoufa, A. Ghith, F. Fayala, Effect of knitting structure and dyeing process on drying time, air and vapor permeability, Text. Res. J. 94 (2024) 1263–1278, https://doi.org/10.1177/0040517524122.
[65] B. Xu, Z. Cai, Fabrication of a superhydrophobic ZnO nanorod array film on cotton fabrics via a wet chemical route and hydrophobic modification, Appl. Surf. Sci. 254 (2008) 5899–5904, https://doi.org/10.1016/j.apsusc.2008.03.160.
[66] P.J. Rivero, A. Urrutia, J. Goicoechea, F.J. Arregui, Nanomaterials for functional textiles and fibers, Nanoscale Res. Lett. 10 (2015) 501, https://doi.org/10.1186/s11671-015-1195-6.
[67] Y. Su, V.G. Kravets, S.L. Wong, J. Waters, A.K. Geim, R.R. Nair, Impermeable barrier films and protective coatings based on reduced graphene oxide, Nat. Commun. 5 (2014) 4843, https://doi.org/10.1038/ncomms5843.
[68] C. Fu, X. Xu, G.-Z. Yin, B. Xu, P. Li, B. Ai, Z. Zhai, F. Gao, J. Zhai, D.-Y. Wang, Surface engineering for cellulose as a boosted Layer-by-Layer assembly: excellent flame retardancy and improved durability with introduction of bio-based “molecular glue”, Appl. Surf. Sci. 585 (2022) 152550 https://doi.org/10.1016/j.apsusc.2022.152550.